Nano Energy 25 (2016) 145–153

Contents lists available at ScienceDirect

Nano Energy

journal homepage: www.elsevier.com/locate/nanoen

Self-sacrificed synthesis of three-dimensional $Na_3V_2(PO_4)_3$ nanofiber network for high-rate sodium–ion full batteries

Wenhao Ren, Zhiping Zheng, Chang Xu, Chaojiang Niu, Qiulong Wei, Qinyou An *, Kangning Zhao, Mengyu Yan, Mingsheng Qin, Liqiang Mai *

State Key Laboratory of Advanced Technology for Materials Synthesis and Processing, Wuhan University of Technology, Wuhan 430070, China

ARTICLE INFO

Article history:
Received 20 February 2016
Received in revised form
18 March 2016
Accepted 27 March 2016
Available online 21 April 2016

Keywords:
Self-sacrificed
$Na_3V_2(PO_4)_3$
Nanofiber network
Sodium–ion
Full batteries

ABSTRACT

The morphological optimization of $Na_3V_2(PO_4)_3$ (NVP) material has a great significance for improving the electrochemical performance since NVP suffers from intrinsic low electronic conductivity. For this purpose, a novel 3D NVP nanofiber network is controllably constructed *via* a facile self-sacrificed template method. Based on time-dependent experiments, an outside-in morphological evolution mechanism from microsphere to 3D nanofiber network is proposed. The as-synthesized material exhibits excellent cyclability (95.9% capacity retention over 1000 cycles at 10 C) and enhanced high-rate performance (94 mA h g^{-1} at 100 C) for sodium half cell. Notably, when evaluated as full battery ($NaTi_2(PO_4)_3$ as anode) cathode, it also shows outstanding cycling stability (96.9% capacity retention over 300 cycles at 5 C) and superior rate capability (80 mA h g^{-1} at 50 C). Such remarkable performance is attributed to the 3D nanofiber network structure, which provides multi-channel ionic diffusion pathway, continuous electronic conduction, and improved structural integrity. This self-sacrificed template strategy presented here can inspire new thought in constructing novel nanofiber/nanowire structures and accelerate the development of high-power sodium–ion batteries.

© 2016 Elsevier Ltd. All rights reserved.

1. Introduction

Lithium ion batteries (LIBs) are regarded as one of the most promising candidates for highly efficient energy storage devices owing to its excellent electrochemical performance [1,2]. However, with the expanding demand for high-performance energy storage systems, there is a rising concern whether the lithium resource could support the large-scale application [3]. As sodium is a low-cost element and shows similar chemical properties to lithium, sodium–ion batteries (SIBs) have also been investigated as a promising alternative in future battery technologies [4–8]. Nevertheless, the rate capability and cyclic ability of SIBs still remain unsatisfactory due to the big ionic radius of Na^+ (1.06 Å) and large volume change during Na^+ intercalation/deintercalation [9–11]. Therefore, exploring suitable electrode materials with robust structure and enough lattice interspaces is in the prior consideration before widespread applications.

As a typical material with NASICON (Na^+ superionic conductor) structure, NVP has received extensive attention in SIBs owing to the highly covalent three dimensional open frameworks, which provides high ionic conductivity and large interspaces [12–14]. Besides, NVP exhibits two different flat voltage plateaus at around 3.4 V and 1.6 V, and has been investigated as both half and symmetric batteries [15]. However, there is only one Na^+ can be insertion/deinsertion during cycling at 1.6 V which leads to a low theoretical capacity (~58 mA h g^{-1}), and the researches with regard to sodium ion full batteries (SIFBs) are far from sufficient for NVP as well as other materials [16–24]. Li *et al.* [16] reported a symmetric NVP battery with the capacity retention of approximately 80% after 200 cycles at 1 C. Wang *et al.* [19] reported a new $Na_{0.66}[Li_{0.22}Ti_{0.78}]O_2 \| Na_3V_2(PO_4)_3$ SIFBs with a discharge capacity of 80 mA h g^{-1} at 1 C. It is clear that the overall electrochemical performance especially high-rate capability and cycling stability of NVP based SIFBs is not encouraging. More systematical explorations are urgently needed to improve the rate performance and cycling stability of NVP based SIFBs.

In addition, the NVP electrodes still suffer from poor electronic conductivity due to the phosphate components [15–17]. Recently, a series of methods have been applied to improve the conductivity and thus the rate capability of NVP, such as hierarchical carbon coating [25], graphene modification [26,27], and mesoporous carbon decoration [28]. Nevertheless, the overwhelming majority of researches have been focused on the carbon coating strategy, while the morphological and structural construction for NVP material, which considered as another effective way for improving its

* Corresponding authors.
E-mail addresses: anqinyou@whut.edu.cn (Q. An), mlq518@whut.edu.cn (L. Mai).

http://dx.doi.org/10.1016/j.nanoen.2016.03.018
2211-2855/© 2016 Elsevier Ltd. All rights reserved.

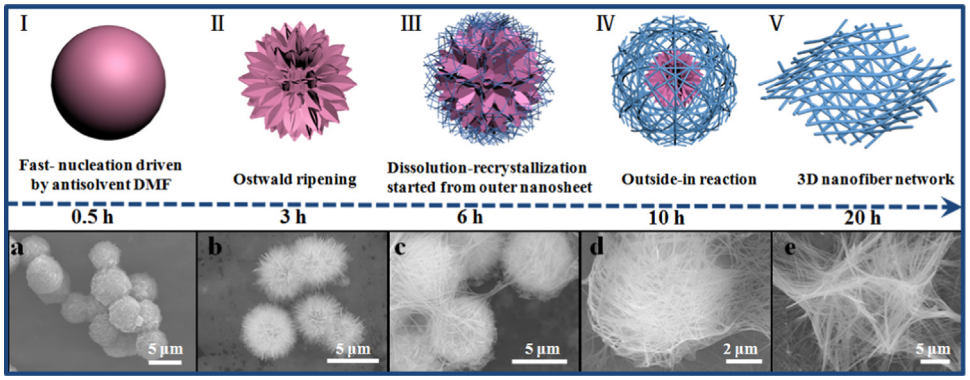

Fig. 1. Schematic illustrations of the time-dependent solvothermal reaction: self-sacrificed evolution mechanism from microsphere to nanofiber network.

electronic conductivity and structural stability, is ignored. Among the various attractive structures, one dimensional (1D) nanomaterials which possess large electrode-electrolyte contact area and short diffusion distance have gained great attention [29–33]. Particularly, 3D architectures built from 1D nanomaterials, such as nanofiber network, not only provide large specific surface area for fast ion diffusion, but also possess improved structural integrity to avoid agglomeration during charge and discharge [34,35]. However, so far, the template-free synthesis of NVP nanowire/nanofiber is still a great challenge and rarely reported. Thus, the rational synthesis of NVP nanofiber network is of great significance.

Herein, we for the first time propose a facile self-sacrificed route to synthesize 3D NVP nanofiber network, and initially develop a $Na_3V_2(PO_4)_3$–$NaTi_2(PO_4)_3$ sodium–ion full battery. Based on time-dependent experiments, a continuous outside-in morphological evolution mechanism from microsphere to 3D nanofiber network is proposed (Fig. 1). When evaluated as half cell cathode, the as-synthesized NVP exhibits outstanding cyclability (95.9% capacity retention over 1000 cycles at 10 C) and enhanced high-rate performance (94 mA h g^{-1} at 100 C). Remarkably, when evaluated as full battery cathode, it also shows excellent cycling stability (96.9% capacity retention over 300 cycles at 5 C) and superior rate capability (80 mA h g^{-1} at 50 C). This is attributed to the combined electrochemical and mechanical advantages of the 3D NVP nanofiber network, which provides fast pathways for Na ion diffusion, large electrode–electrolyte contact area, excellent strain adaptation and superior structural integrity.

2. Experimental section

2.1. Material synthesis

Synthesis of $Na_3V_2(PO_4)_3$/C nanofiber network (NVP-F): V_2O_5, $H_2C_2O_4 \cdot 2H_2O$ and NaH_2PO_4 were analytical grade and purchased from the Sinopharm Chemical Reagent Co., Ltd. (Shanghai, China). First, V_2O_5 (1 mmol) were added in 30 ml *n*-dimethylformamide (DMF) with stirring at 80 °C for 0.5 h. Then, NaH_2PO_4 (3 mmol), $H_2C_2O_4 \cdot 2H_2O$ (3 mmol) and 5 ml water were dissolved in above solution and vigorously stirred for another 0.5 h. After that, the solution was transferred into a 50 ml Teflon-lined stainless steel autoclave and kept at 180 °C for 20 h. Then, the products were collected and the glucose was added in the solution to realize a molar ratio of $Na_3V_2(PO_4)_3$: glucose=1:1. The solution was then stirred for 0.5 h to get a homogeneous precursor followed by drying at 70 °C in an air oven. In the end, the $Na_3V_2(PO_4)_3$ nanofiber network was obtained from the precursor *via* preheating it at 400 °C for 4 h followed by annealing at 700 °C for 8 h in argon atmosphere with a heating rate of 5 °C min^{-1}.

2.2. Materials characterization

XRD measurement was performed to investigate the crystallographic information using a D8 Advance X-ray diffractometer with non-monochromated Cu Kα X-ray source. The property of carbon layer was analyzed with INVIA Raman Spectroscopy. FESEM images were collected with a JEOL JSM-7100F at an acceleration voltage of 10 kV. TEM and HRTEM images were recorded with a JEM-2100F microscope. Raman spectra were obtained using a Renishaw INVIA micro-Raman spectroscopy system. BET surface areas were measured using Tristar II 3020 instrument by nitrogen adsorption of at 77 K. Carbon content analysis was determined by Vario EL cube CHNSO elemental analyzer.

2.3. Measurement of electrochemical performance

The electrochemical measurements were tested with 2016 coin cells assembled in a glove box filled with pure argon gas. For SIBs, sodium metal was used as the anode, a 1 M solution of $NaClO_4$ in ethylene carbon (EC)–dimethyl carbonate (DMC) (1: 1 w/w) and 5% FEC was used as the electrolyte, and a Whatman Glass Microfibre Filter (Grade GF/F) was used as the separator. The cathode/anode was made by dispersing 70 wt% active material, 20 wt% carbon black, and 10 wt% PVDF in *N*-methyl pyrrolidone (NMP) with stirring for 0.5 h. Then, the cathode/anode slurry was coated uniformly on Al/Cu foil and dried overnight at 70 °C to yield the working electrodes. The battery was aged for 24 h before test to ensure full absorption of the electrolyte into the electrodes. The mass loading of the active material was 1.5–2 mg cm^{-2}. Galvanostatic charge/discharge measurements were performed with a multichannel battery testing system (LAND CT2001A), where 1 C equals to 118 mA h g^{-1} (theoretical capacity). Cyclic voltammetry (CV) and electrochemical impedance spectroscopy (EIS) were performed with an electrochemical workstation (Autolab PGSTAT302N).

3. Results and discussion

The detailed morphologies and structures of the solvothermally prepared samples were characterized by scanning electron microscopy (SEM) and transmission electron microscopy (TEM). The schematic illustrations combined with time-dependent experiments were carried out to investigate the morphological evolution mechanism from microflower to 3D nanofiber network structure (Fig. 1). As shown in Fig. 1(a), the fast nucleation and crystal growth processes lead to the formation of the original NVP microspheres with diameter of 3–5 μm when the solvothermal time is 0.5 h. During this process, the DMF serves as an antisolvent and decreases the solubility of the inorganic salts, creating a facile

nucleation condition [15,36]. After solvothermal reaction time is prolonged to 3 h, the surface of microspheres are converted into nanosheet-assembled microflower *via* Ostwald ripening. The microflowers have a diameter of 3–5 μm and the nanosheet building blocks show a thickness of 20–50 nm (Fig. 1(b)) [37,38]. As the time increased further, the metastable nanosheets on the surface are served as the self-sacrificed template and dissolve-recrystallized into nanofibers (Fig. 1(c)) due to the accessibility to the reaction medium [39,40]. This may attributed to the electrophilic and nucleophilic properties of DMF, which served as the source of intermediates mediating ingredient and create a reaction impetus to promote the dissolution-recrystallization process [41,42]. Control experiments (Fig. S1) with pure water or pure DMF as the solvents were also carried out, and none of them can lead to the formation of nanofibers. As the reaction time increases to 10 h, more nanofiber forms followed by the consumption of microflowers, and the microflower structure are embedded in the nanofiber network (Fig. 1(d)). Upon further prolongation of the reaction time, the dissolution-recrystallization process in the inner region of microflower structure continues and the nanofiber networks become more and more dense. Finally, the entire microflower is evolved into 3D nanofiber network structure as the solvothermal time is increased to 20 h. The resultant nanofibers have diameters of 20–80 nm and lengths up to several millimeters (Fig. 1(e)). Notably, the detailed evolution process from microflower to 3D nanofiber network is systematically presented in Fig. S2.

Significantly, both the nanofiber network (Fig. 2(C)) and microflower (Fig. S3) are maintained very well even after calcinated at 700 °C (designated as NVP-F and NVP-M). The accompanying energy dispersive spectrometry (EDS) element mappings indicate that Na, P, V, and C are homogeneously distributed in NVP-F. The well-interconnected network structure of NVP-F can be clearly observed from TEM images (Fig. 2(d) and S4). The lattice fringes of

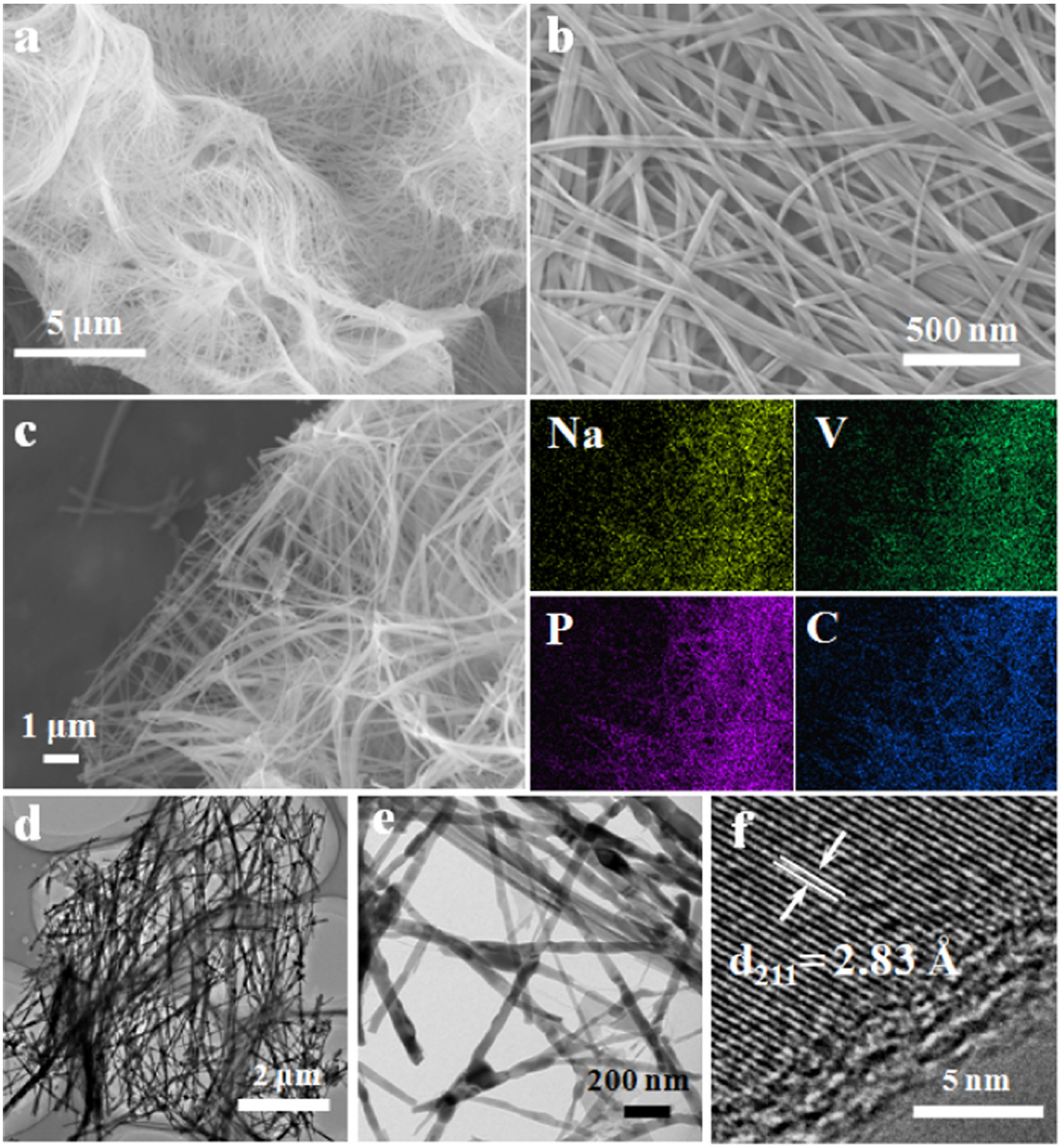

Fig. 2. SEM images of NVP-F before (a,b) and after (c) annealing. The accompanying diagram of (c) is the corresponding EDS elemental mapping. TEM (d,e) and HRTEM (f) images of NVP-F.

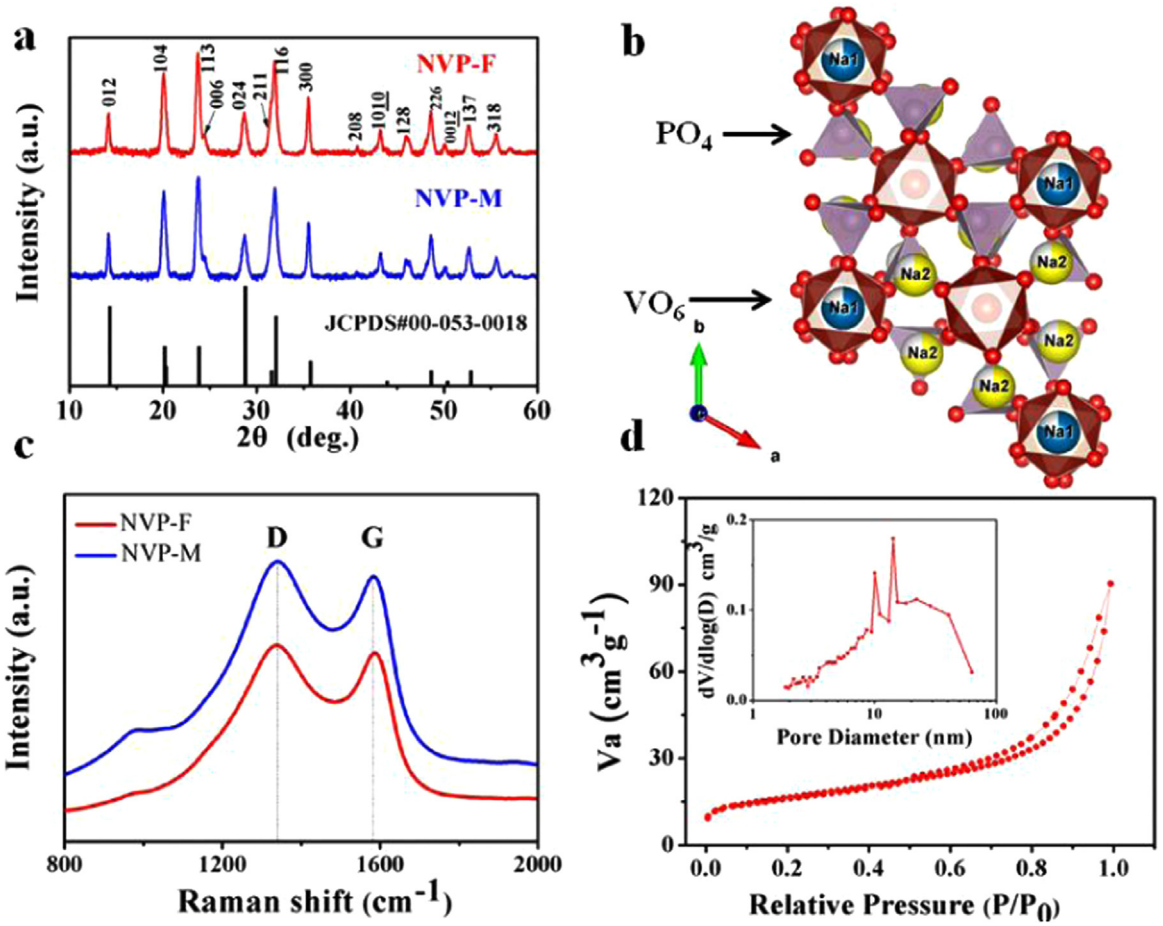

Fig. 3. XRD patterns (a), crystal structure (b), Raman spectrum (c), nitrogen adsorption–desorption isotherm (d) and corresponding pore size distribution (inset) of NVP.

NVP-F (Fig. 2(f)) and NVP-M (Fig. S3d) with *d*-spacings of around 2.8 and 3.7 Å can be clearly observed, correspond to the (211) and (113) interplanes of NVP, respectively. Notably, a uniform thin carbon layer of around 4 nm covers the surface of NVP nanofibers (Fig. 2(f)), which in turn verifies the effectiveness of the carbon coating strategy.

The X-ray diffraction (XRD) measurements were conducted to determine the phase structure of NVP-F and NVP-M. The crystal structures of the samples after solvothermal reaction for 3, 10 and 20 h (Fig. S5) are partially crystallized and cannot form the NVP phase. After annealing, all the prepared materials are well indexed to the NASICON structured NVP with a $R\bar{3}c$ space group (JCPDS card No. 00–053–0018), which is consistent with previous reports [43,44]. Moreover, the peak positions and intensities of sample NVP-F and NVP-M are similar, which suggests that the morphology does not significantly change the crystal structure and crystallinity of NVP (Fig. 3(a)). As shown in Fig. 3(b), the NVP structure is established on a 3D framework of VO_6 octahedra sharing all the corners with PO_4 tetrahedra. There exist two different Na atoms which located at Na_1 (sixfold coordination) and Na_2 (eightfold coordination) sites. When Na ions is extracted from $Na_3V_2(PO_4)_3$ to form $NaV_2(PO_4)_3$, only Na ions located at Na_2 site can be extracted, and the rest of Na ions still remain at Na_1 site to maintain the basic structure [45]. The Raman spectras (Fig. 3(c)) of NVP-F and NVP-M display two characteristic bands of carbonaceous materials located at 1337 cm^{-1} (D-band, disorder carbon) and 1587 cm^{-1} (G-band, crystalline graphitized carbon). The peak intensity ratio of D to G band (I_D/I_G) is 1.01 and 1.05 for NVP-F and NVP-M, indicating a relatively high degree of graphitization [46]. The carbon contents of NVP-F and NVP-M are 6.5 wt% and 6.7 wt%, respectively, which were characterized by CHNSO elemental analyzer. The surface area and pore structure of NVP-F (Fig. 3(d)) and NVP-M (Fig. S6) were determined through Brunauer–Emmett–Teller (BET) test. The BET surface area increased from 48.2 to 56.1 $m^2 g^{-1}$ after the morphological evolution from microflower to nanofiber network, indicating the large effective contact area provided by the unique structure. The main pore-size distribution of NVP-F is around 10–20 nm, which demonstrates that the 3D nanofiber network structure indeed produces some voids and interspaces to achieve stress adaptation. To further investigate the oxidation state of vanadium in NVP-N, X-ray photoelectron spectrum (XPS) (Fig. S7) measurement is adopted. The calibrated binding energy of dominant peak locates at 516.88 eV, which corresponds to $V^{3+}$and no higher oxidation state is observed [15].

The electrochemical measurements were conducted to investigate the sodium storage performance in half cell. The cyclic voltammetry (CV) (Fig. 4(a)) was conducted at a potential window between 2.3 and 3.9 V versus Na^+/Na at a scan rate of 0.1 mV s^{-1}. As illustrated in the CV profiles, a pair of well-defined redox peaks appear on both electrodes, corresponding to the reversible transformation of V^{3+}/V^{4+} [12,15]. The potential interval between the cathodic and anodic peaks of NVP-F and NVP-M are 128 mV and 231 mV, respectively, indicating the lower polarization of NVP-F electrodes. Furthermore, the peak current of NVP-F is obviously higher than NVP-M, demonstrating the faster kinetics enhanced by the higher ion/electron conduction [28]. Fig. 4(b) and (c) display the rate performance and corresponding charge–discharge curves of NVP-F and NVP-M from 1 C to 100 C. Notably, the reversible capacity of 113, 110, 108, 102, 98 mA h g^{-1} can be obtained for NVP-F at a current density of 1, 5, 10, 30 and 50 C, respectively.

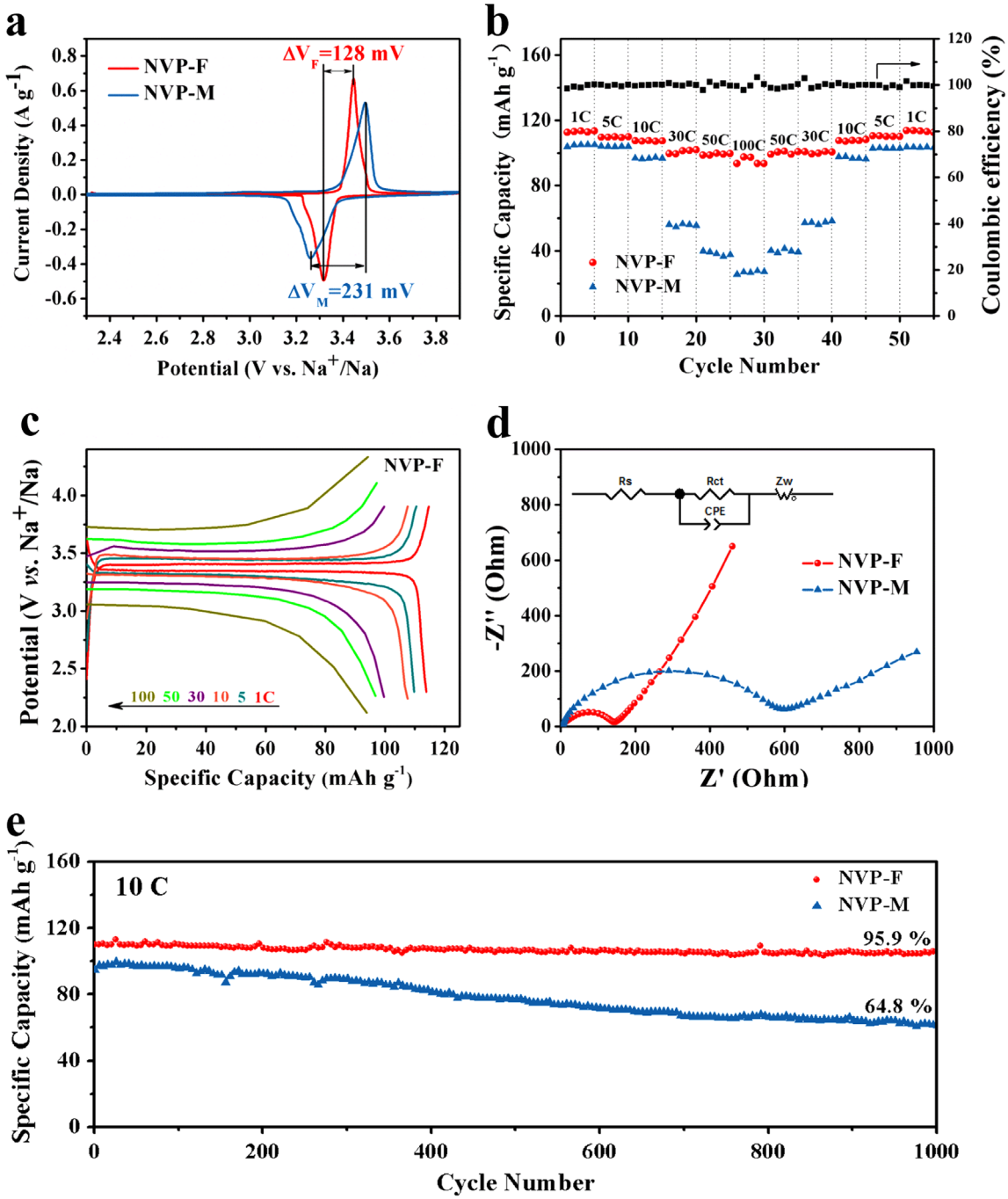

Fig. 4. Electrochemical properties of NVP-F and NVP-M as half cell cathodes. (a) The CV curves of NVP-F and NVP-M electrodes at a scan rate of 0.1 mV s^{-1}. (b) Rate capability of the NVP-F and NVP-M electrodes. (c) Galvanostatic charge-discharge curves of NVP-F at various current rates from 1 C to 100 C (d) The Nyquist plots of the NVP-F and NVP-M electrodes after three full cycles at 1 C with equivalent circuit inset. (e) Cycling performance of the NVP-F and NVP-M at 10 C.

Obviously, the NVP-F exhibits much higher capacity at each rate compared with NVP-M and still delivers a specific discharge capacity of 94 mA h g^{-1} even at 100 C, approximately 83% of the reversible capacity at 1 C. When the current density comes back to 1 C again, the specific capacity of 113 mA h g^{-1} (95.7% of its theoretical capacity) could be recovered for the NVP-F electrode. The advantages of 3D nanofiber network structure are further verified *via* the electrochemical impedance spectroscopy (EIS) comparison between NVP-F and NVP-M electrodes (Fig. 4(d)). Before the EIS test, the cells were charged to 3.9 V and then kept for a period of time to reach a stable state. The charge transfer resistance (R_{ct}) of the NVP-F cathode is 149 Ω, which is much smaller than that of NVP-M (610 Ω), demonstrating the lower polarization of NVP-F. The suppression of R_{ct} further confirms that the 3D network structure indeed supplies continuous electronic pathway and improves the charge transfer kinetics. Moreover, the slanted line at low frequency represents the Warburg impedance (Z_w), which indicates the sodium diffusion process within the electrode. Thus, the larger slope coefficient of NVP-F represents the better sodium diffusion among the electrodes compared with NVP-M [33,47,48]. The long-term cyclability of NVP-F and NVP-M is further performed in Fig. 4(e). The NVP-F and NVP-M cathodes deliver the initial specific discharge capacity of 110 and 100 mA h g^{-1} at 10 C, respectively. After 1000 cycles, the capacity retention of NVP-F electrodes maintain at 95.9%, which is much higher than that of NVP-M (64.8%). The corresponding charge/discharge curves of

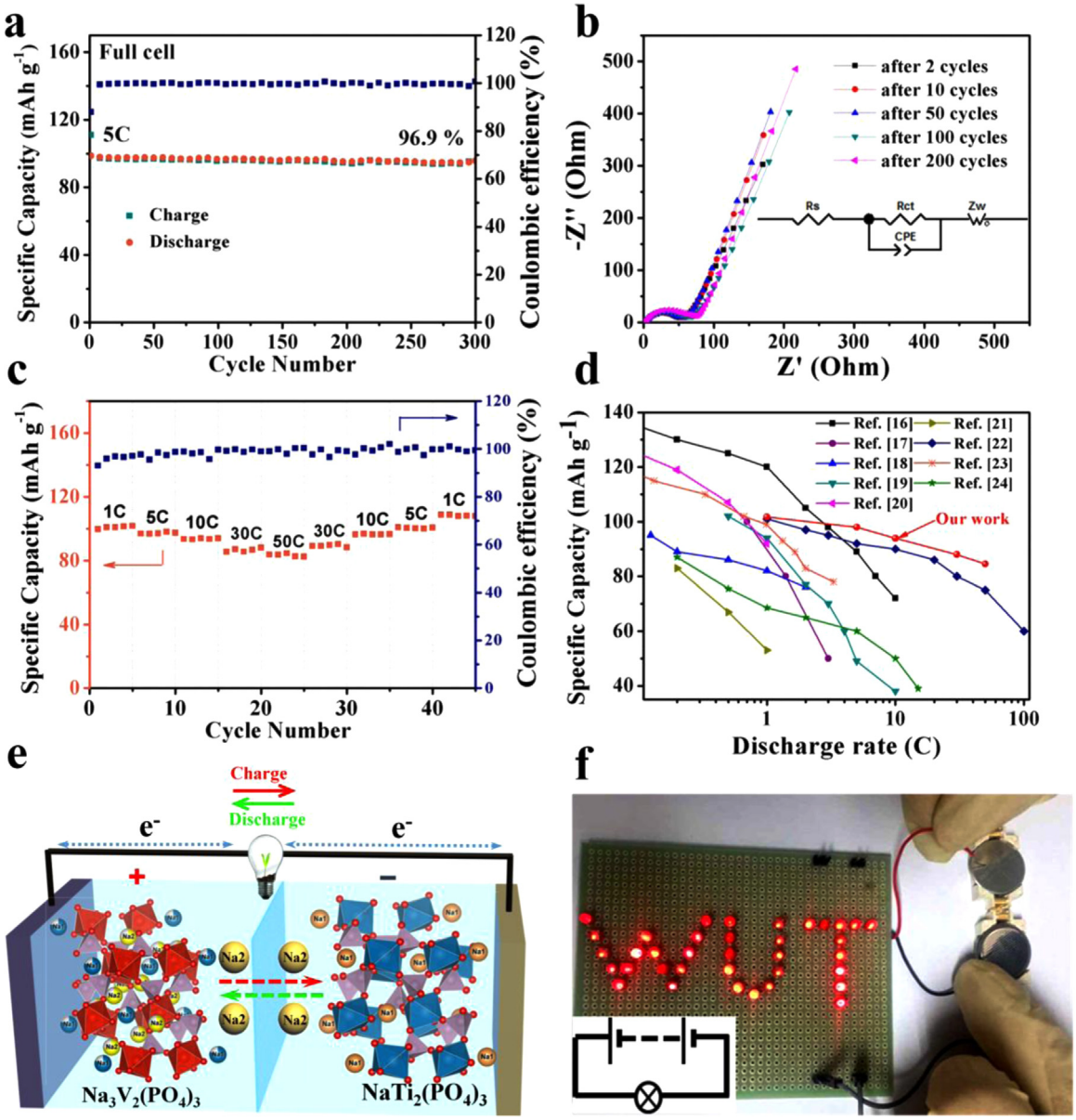

Fig. 5. Electrochemical properties of NVP-F as full cell cathode. (a) The cycling performance and its corresponding coulombic efficiency of NVP-F. (b) The Nyquist plots of NVP-F after different cycles at 5 C with equivalent circuit inset. (c) Rate capability of the NVP-F. (d) Comparison of rate performance to recently reported sodium–ion full cells. (e) Schematic illustration of the Na_2-to-Na_2 insertion/deinsertion between NVP and NTP. (f) The lighted LED bulbs driven by the full cell.

NVP-F (Fig. S8) at 2, 100, 500 and 1000 cycles show that no obvious polarization and capacities decay are observed, indicating excellent structural stability. It is clear that the overall electrochemical performance of NVP-F is much better than NVP-M, and the NVP-F exhibits great competitiveness compared with state-of-art research results [25,26,28].

The sodium–ion full batteries based on NVP-F, $NaTi_2(PO_4)_3$ (NTP) and electrolyte (NVP‖1 M $NaClO_4$/EC+DMC+FEC‖NTP) are also fabricated. The detailed electrochemical behaviors with respect to the cathode weight are shown in Fig. 5. Before full cell assembly, the crystal structure (Fig. S9), morphology (Fig. S10), and electrochemical performance (Fig. S11) of NTP are also presented. The battery system balance was achieved by controlling the electrode capacity ratio of anode/cathode to 1.2. As shown in Fig. 5(a), the NVP-F exhibits 96.9% capacity retention over 300 cycles at the current density of 5 C. The coulombic efficiency, which is crucial for the full cell reaches nearly 100% throughout the cycling, indicating the good reversibility of the SIFBs. The EIS measurements were also carried out in order to investigate the charge transfer and ionic diffusion ability of battery system. As shown in Fig. 5 (b) and Table S1, the charge transfer resistance (R_{ct}) value for full cell at 2nd cycles is quite small (40 Ω) and there is no obvious impedance increase even after 200 cycles, indicating the improved ion/electron transfer kinetics and good electrochemical stability. Fig. 5(c) shows the rate capability of the NVP-F in SIFBs. As the current density increase from 1 to 5, 10, 30, and 50 C, the electrode shows slight capacity decline, varying from 103 to 98, 94, 88, and 80 mA h g^{-1}, respectively. Significantly, when the rate was turned back to 1 C, the reversible capacity can be recovered to 101 mA h g^{-1} again (98% capacity retention), indicating the excellent rate capability. The corresponding charge/discharge curves from 1 C to 50 C are shown in Fig. S12. Notably, the over potential for full cell is less than 50 mV at 1 C rate, indicating slight polarization and fast chemical kinetics between the cathode and anode. The Ragone plots (Fig. S13) are applied to display the relationship between energy density and power density of full cell. There is no

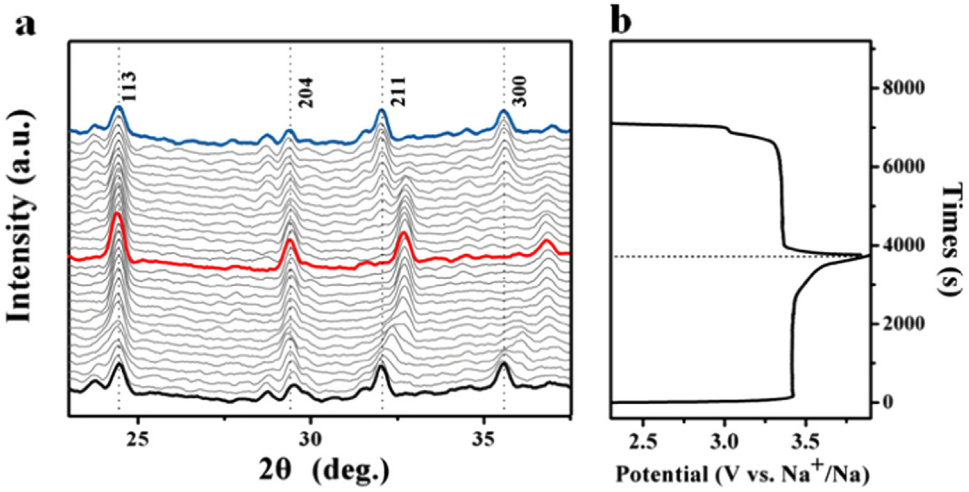

Fig. 6. (a) The *in situ* XRD patterns of NVP-F for a full charge–discharge cycle in a voltage range of 2.3–3.9 V. (b) The corresponding time-potential curve.

obvious trend for energy density decrease with the power density increasing. Most importantly, the energy density still reaches up to 90 Wh kg^{-1} even at a power density as high as 6 kW kg^{-1}. We further compared the rate performance of recently reported sodium–ion full cells to highlight the competitiveness of the full cell (Fig. 5(b)). To the best of our knowledge, NVP-F shows the optimum electrochemical performance in terms of combined high rate capability and long-term cycling stability in sodium–ion full cells. Most importantly, the above electrochemical performance of NVP-F is even better than many recently reported materials in lithium ion full cells [49–51], demonstrating the potential for large scale energy storage applications. Fig. 5(e) displays the schematic diagram of the Na_2-to-Na_2 ionic conduction between $Na_3V_2(PO_4)_3$ and $NaTi_2(PO_4)_3$ during charge/discharge. The corresponding lighted LED bulbs indicate that our full cell can work normally after fully charged (Fig. 5(f)).

Furthermore, the crystal structure evolution of NVP-F during Na ion insertion/deinsertion process was investigated through *in situ* XRD technique (Fig. 6). The prepared NVP-F *in situ* cell was charged to 3.9 V and then discharged to 2.3 V at the current density of 100 mA h g^{-1}, with 2θ recorded from 23° to 37.5°. All the diffraction peaks can be indexed to either the Na-rich $Na_{3-\alpha}V_2(PO_4)_3$ phase or the Na-poor $Na_\beta V_2(PO_4)_3$ phase. As expected, $Na_{3-\alpha}V_2(PO_4)_3$ peaks disappear on charge and are restored on discharge; conversely, $Na_\beta V_2(PO_4)_3$ peaks start to form and grow on charge and disappear on discharge. It is clear that the (211) and (300) peaks shift to higher angles during charge process, indicating that the *d*-spacings decrease during the Na ions deinsertion. After recharging to 3.9 V, the peaks return to the original positions, indicating the good reversibility. Moreover, overcharge tolerance of the material is also another important property which should be discussed before practical applications. For overcharge tests, the NVP-F electrodes were firstly charged to 4.7 V (Fig. S14), and then cycled between 2.3 and 3.9 V at 5 C. The initial charge/discharge capacities of NVP-F are 181.8 and 127.6 mA h g^{-1}, respectively. Notably, after 100 cycles, the electrodes display excellent cycling performance, with capacity retention above 110 mA h g^{-1}, suggesting good overcharge stability.

The above enhanced electrochemical performance of NVP-F is attributed to the 3D nanofiber network structure with optimized electrochemical and mechanical features as shown in Fig. S15. In terms of electrochemical aspect, the 3D nanofiber network produces more interspace and voids to create the stable multi-channel pathway for Na ion insertion/deinsertion. The enlarged surface area of NVP-F further facilitates the effective contact between active materials and electrolyte, resulting in promoted reaction kinetics. Besides, the interconnected structure offers continuous electron conduction which is crucial for reducing the impedance of NASICON-type NVP electrodes, thus leading to high rate capability. From the mechanics point of view, the framework structure constructed through interconnected nanofiber network can achieve stress relaxation and effectively prevent the self-aggregation of nanofibers. It is clear that the nanofiber network structure is still maintained even after 100 cycles at 5 C (Fig. S16). Thus, the improved charge transfer and ionic diffusion kinetics can be maintained throughout the cycling owing to the stable structural integrity.

4. Conclusion

We developed a facile self-sacrificed template route to fabricate novel 3D $Na_3V_2(PO_4)_3$ nanofiber network. An outside-in morphological evolution mechanism from microsphere to 3D nanofiber network is proposed. This network structure, which provides multi-channel diffusion pathways, continuous electronic conduction, and superior structure integrity, possesses both electrochemical and mechanical advantages. The as-prepared NVP-F electrodes display outstanding rate capability (94 mA h g^{-1} at 100 C for half cell, 80 mA h g^{-1} at 50 C for full battery) and unprecedented cycling stability (95.9% capacity retention at 10 C after 1000 cycles for half cell, 96.9% capacity retention over 300 cycles at 5 C for full battery). Such remarkable electrochemical behavior of NVP-F is among the most attractive performance for all recently reported SIFBs, and exhibits great potential for high-power and long-life energy storage applications.

Acknowledgments

This work was supported by the National Basic Research Program of China (2013CB934103, 2012CB933003), the International Science & Technology Cooperation Program of China (2013DFA50840), the National Natural Science Foundation of China (51302203, 51272197, 51521001), the Hubei Province Natural Science Fund for Distinguished Young Scholars (2014CFA035), the National Natural Science Fund for Distinguished Young Scholars (51425204), and the Fundamental Research Funds for the Central Universities (WUT: 2015-III-021, 2015-III-032, 2015-III-052, 2015-PY-2). We are deeply thankful to Professor Dongyuan Zhao of Fudan University for stimulating discussion and kind help.

Appendix A. Supporting information

Supplementary data associated with this article can be found in the online version at http://dx.doi.org/10.1016/j.nanoen.2016.03.018.

References

[1] Z. Yang, J. Zhang, M.C.W. Kintner-Meyer, X. Lu, D. Choi, J.P. Lemmon, J. Liu, Chem. Rev. 111 (2011) 3577–3613.
[2] J. Liu, Adv. Funct. Mater. 23 (2013) 924–928.
[3] J.B. Goodenough, K.S. Park, J. Am. Chem. Soc. 135 (2013) 1167–1176.
[4] N. Yabuuchi, K. Kubota, M. Dahbi, S. Komaba, Chem. Rev. 114 (2014) 11636–11682.
[5] S.W. Kim, D.H. Seo, X. Ma, G. Ceder, K. Kang, Adv. Energy Mater. 2 (2012) 710–721.
[6] C. Zhu, P. Kopold, P. van Aken, J. Maier, Y. Yu, Adv. Mater. (2016), http://dx.doi.org/10.1002/adma.201505943.
[7] M.D. Slater, D. Kim, E. Lee, C.S. Johnson, Adv. Funct. Mater. 23 (2013) 947–958.
[8] D. Kundu, E. Talaie, V. Duffort, L.F. Nazar, Angew. Chem. 54 (2015) 3431–3448.
[9] H. Pan, Y.S. Hu, L. Chen, Energy Environ. Sci. 6 (2012) 2338–2360.
[10] V. Palomares, P. Serras, I. Villaluenga, K.B. Hueso, J. Carretero-González, T. Rojo, Energy Environ. Sci. 5 (2012) 5884–5901.
[11] N. Yabuuchi, M. Kajiyama, J. Iwatate, H. Nishikawa, S. Hitomi, R. Okuyama, R. Usui, Y. Yamada, S. Komaba, Nat. Mater. 11 (2012) 512–517.
[12] C. Zhu, K. Song, P.A. van Aken, J. Maier, Y. Yu, Nano Lett. 14 (2014) 2175–2180.
[13] J.N. Chotard, G. Rousse, R. David, O. Mentre, M. Courty, C. Masquelier, Chem. Mater. 27 (2015) 5982–5987.
[14] W. Zhang, Y. Liu, C. Chen, Z. Li, Y. Huang, X. Hu, Small (2015).
[15] Q. An, F. Xiong, Q. Wei, J. Sheng, L. He, D. Ma, Y. Yao, L. Mai, Adv. Energy Mater. 5 (2015).
[16] S. Li, Y. Dong, L. Xu, X. Xu, L. He, L. Mai, Adv. Mater. 26 (2014) 3545–3553.
[17] S.M. Oh, S.T. Myung, C.S. Yoon, J. Lu, J. Hassoun, B. Scrosati, K. Amine, Y.K. Sun, Nano Lett. 14 (2014) 1620–1626.
[18] Y. Dong, S. Li, K. Zhao, C. Han, W. Chen, B. Wang, L. Wang, B. Xu, Q. Wei, L. Zhang, X. Xu, L. Mai, Energy Environ. Sci. 8 (2015) 1267–1275.
[19] Y. Wang, X. Yu, S. Xu, J. Bai, R. Xiao, Y.S. Hu, H. Li, X.Q. Yang, L. Chen, X. Huang, Nat. Commun. 4 (2013).
[20] D. Kim, E. Lee, M. Slater, W. Lu, S. Rood, C.S. Johnson, Electrochem. Commun. 18 (2013) 66.
[21] S. Guo, H. Yu, P. Liu, Y. Ren, T. Zhang, M. Chen, M. Ishida, H. Zhou, Energy Environ. Sci. 8 (2015) 1237–1244.
[22] C.Y. Yu, J.S. Park, H.G. Jung, K.Y. Chung, D. Aurbach, Y.K. Sun, S.T. Myung, Energy Environ. Sci. 8 (2015) 2019–2026.
[23] L. Wang, J. Song, R. Qiao, L.A. Wray, M.A. Hossain, Y.D. Chuang, W. Yang, Y. Lu, D. Evans, J.J. Lee, S. Vail, X. Zhao, M. Nishijima, S. Kakimoto, J.B. Goodenough, J. Am. Chem. Soc. 137 (2015) 2548–2554.
[24] S. Guo, P. Liu, Y. Sun, K. Zhu, J. Yi, M. Chen, M. Ishida, H. Zhou, Angew. Chem. 54 (2015) 11701–11705.
[25] Y. Fang, L. Xiao, X. Ai, Y. Cao, H. Yang, Adv. Mater. 27 (2015) 5895–5900.
[26] X. Rui, W. Sun, C. Wu, Y. Yu, Q. Yan, Adv. Mater. 27 (2015) 6670–6676.
[27] Y.H. Jung, C.H. Lim, D.K. Kim, J. Mater. Chem. A 1 (2013) 11350–11354.
[28] Y. Jiang, Z. Yang, W. Li, L. Zeng, F. Pan, M. Wang, X. Wei, G. Hu, L. Gu, Y. Yu, Adv. Energy Mater. 5 (2015).
[29] J. Liu, K. Tang, K. Song, P.A. van Aken, Y. Yu, J. Maier, Nanoscale 6 (2014) 5081–5086.
[30] L. Mai, X. Tian, X. Xu, L. Chang, L. Xu, Chem. Rev. 114 (2014) 11828–11862.
[31] X. Wang, C. Niu, J. Meng, P. Hu, X. Xu, X. Wei, L. Zhou, K. Zhao, W. Luo, M. Yan, Adv. Energy Mater. 5 (2015).
[32] L. Zhang, K. Zhao, W. Xu, J. Meng, L. He, Q. An, X. Xu, Y. Luo, T. Zhao, L. Mai, RSC Adv. 4 (2014) 33332–33337.
[33] H. Li, Y. Bai, F. Wu, Y. Li, C. Wu, J. Power Sources 273 (2015) 784–792.
[34] W. Ren, Z. Zheng, Y. Luo, W. Chen, C. Niu, K. Zhao, M. Yan, L. Zhang, J. Meng, L. Mai, J. Mater. Chem. A 3 (2015) 19850–19856.
[35] X. Fang, M. Ge, J. Rong, C. Zhou, ACS Nano 8 (2014) 4876–4882.
[36] D. Duffy, M. Barrett, B. Glennon, Cryst. Growth Des. 13 (2013) 3321–3332.
[37] J.S. Chen, L.A. Archer, X.W.D. Lou, J. Mater. Chem. A 21 (2011) 9912–9924.
[38] P.W. Voorhees, J. Stat. Phys. 38 (1985) 231–252.
[39] Y. Wu, A. Islam, X. Yang, C. Qin, J. Liu, K. Zhang, W. Peng, L. Han, Energy Environ. Sci. 7 (2014) 2934–2938.
[40] Y. Ma, B. Ding, G. Ji, J.Y. Lee, ACS Nano 7 (2013) 10870–10878.
[41] S. Ding, N. Jiao, Angew. Chem. 51 (2012) 9226–9237.
[42] J. Muzart, Tetrahedron 65 (2009) 8313–8323.
[43] Z. Jian, W. Han, X. Lu, H. Yang, Y.S. Hu, J. Zhou, Z. Zhou, J. Li, W. Chen, D. Chen, Adv. Energy Mater. 3 (2013) 156–160.
[44] K. Saravanan, C.W. Mason, A. Rudola, K.H. Wong, P. Balaya, Adv. Energy Mater. 3 (2013) 444–450.
[45] Z. Jian, C. Yuan, W. Han, X. Lu, L. Gu, X. Xi, Y.-S. Hu, H. Li, W. Chen, D. Chen, Y. Ikuhara, L. Chen, Adv. Funct. Mater. 24 (2014) 4265–4272.
[46] W. Duan, Z. Zhu, H. Li, Z. Hu, K. Zhang, F. Cheng, J. Chen, J. Mater. Chem. A 2 (2014) 8668–8675.
[47] K. Zhao, F. Liu, C. Niu, W. Xu, Y. Dong, L. Zhang, S. Xie, M. Yan, Q. Wei, D. Zhao, Adv. Sci. (2015).
[48] H. Li, X. Yu, Y. Bai, F. Wu, C. Wu, L. Liu, X. Yang, J. Mater. Chem. A 3 (2015) 9578–9586.
[49] P. Xiong, L. Peng, D. Chen, Y. Zhao, X. Wang, G. Yu, Nano Energy 12 (2015) 816–823.
[50] Y. Wang, Y. Wang, D. Jia, Z. Peng, Y. Xia, G. Zheng, Nano Lett. 14 (2014) 1080–1084.
[51] X. Li, J. Liang, Z. Hou, W. Zhang, Y. Wang, Y. Zhu, Y. Qian, J. Power Sources 293 (2015) 868–875.

Wenhao Ren received his B. S. degree in Department of Materials Science and Engineering from Wuhan University of Science and Technology in 2012 and he is currently working toward the pH. D. degree in Material Science at Wuhan University of Technology. His current research involves nanomaterials and devices.

Zhiping Zheng is currently an undergraduate in Wuhan University of Technology. He has learned in WUT-Harvard Joint Nano Key Laboratory for two years under the direct of Professor Mai. His research is focused on synthesis of cathode materials. He shows high interests for fundamental study of materials.

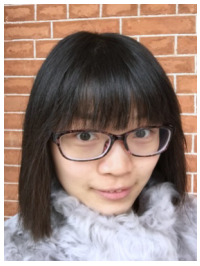

Chang Xu received her B. S. degree in Material Engineering from Shenyang Jianzhu University in 2013. She is currently a senior-grade postgraduate student in WUT-Harvard Joint Nano Key Laboratory at Wuhan University of Technology. Her research is focused on novel nanomaterials used as electrodes of lithium/sodium ion secondary batteries.

Chaojiang Niu received his M. S. degree in Material Chemistry from Wuhan University of Technology in 2009. He is currently working toward the pH. D. degree and his current research focuses on the energy storage materials and devices.

Qiulong Wei received his B. S. degree in Department of Materials Science and Engineering from Wuhan University of Technology in 2011. He has joined State Key Laboratory of Advanced Technology for Materials Synthesis and Processing for four years. He is currently working toward the pH. D. degree. His current research involves the design and synthesis of nanomaterials for achieving both high energy density and power density electrochemical energy storage device, including the lithium–ion battery, sodium ion battery and the hybrid capacitor.

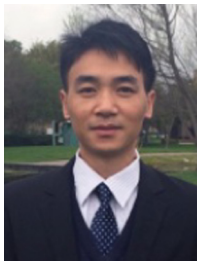

Qinyou An is Associate Professor of Materials Science and Engineering at Wuhan University of Technology (WUT). He received his pH. D. degree from WUT in 2014. He carried out his postdoctoral research in the laboratory of Prof. Yan Yao at the University of Houston in 2014–2015. Currently, his research interest includes energy storage materials and devices.

Kangning Zhao received his B. S. degree in Department of Materials Science of Engineering from Wuhan University of Technology in 2012. He has joined WUT-Harvard Joint Nano Key Laboratory for two years. He is currently working toward the pH. D. degree. His current research involves the nanomaterials achieving high energy density and power density for lithium ion battery and sodium ion battery.

Mengyu Yan received his B. S. degree in Material Chemistry from China University of Geosciences in 2012 and he is currently working toward the pH. D. degree in Material Science at Wuhan University of Technology. His current research interests include nanoenergy materials and devices.

Mingsheng Qin is currently an undergraduate in Wuhan University of Technology. He has learned in WUT-Harvard Joint Nano Key Laboratory for 1 year under the direct of Professor Mai. His research is focused on synthesis of cathode materials. He shows high interests for fundamental study of materials.

Liqiang Mai is Chair Professor of Materials Science and Engineering at Wuhan University of Technology (WUT). He received his pH. D. from WUT in 2004. He carried out his postdoctoral research in the laboratory of Prof. Zhonglin Wang at Georgia Institute of Technology in 2006–2007 and worked as advanced research scholar in the laboratory of Prof. Charles M. Lieber at Harvard University in 2008–2011. His current research interests focus on nanowire materials and devices for energy storage. He received the National Natural Science Fund for Distinguished Young Scholars, the First Prize for Hubei Natural Science Award and so forth. He was selected as National Hundred-Thousand-Ten Thousand Project Leading Talent and granted the honorary title of "Young and Middle-aged Experts with Outstanding Contributions" of China.